JOURNAL OF GEOPHYSICAL RESEARCH, VOL. 111, D13205, doi:10.1029/2005JD006661, 2006

North American and Asian aerosols over the eastern Pacific Ocean and their role in regulating cloud condensation nuclei

G. Roberts,[1] G. Mauger,[1] O. Hadley,[1] and V. Ramanathan[1]

Received 10 September 2005; revised 12 January 2006; accepted 28 March 2006; published 12 July 2006.

[1] Measurements of aerosol and cloud properties in the Eastern Pacific Ocean were taken during an airborne experiment on the University of Wyoming's King Air during April 2004 as part of the Cloud Indirect Forcing Experiment (CIFEX). We observed a wide variety of aerosols, including those of long-range transport from Asia, clean marine boundary layer, and North American emissions. These aerosols, classified by their size distribution and history, were found in stratified layers between 500 to 7500 m above sea level and thicknesses from 100 to 3000 m. A comparison of the aerosol size distributions to measurements of cloud condensation nuclei (CCN) provides insight to the CCN activity of the different aerosol types. The overall ratio of measured to predicted CCN concentration (N_{CCN}) is 0.56 ± 0.41 with a relationship of $N_{CCN,measured} = N_{CCN,predicted}^{0.846\pm0.002}$ for 23 research flights and 1884 comparisons. Such a relationship does not accurately describe a CCN closure; however, it is consistent with our measurements that high CCN concentrations are more influenced by anthropogenic sources, which are less CCN active. While other CCN closures have obtained results closer to the expected 1:1 relationship, the different aerosol types (and presumably differences in aerosol chemistry) are responsible for the discrepancy. The measured N_{CCN} at 0.3% supersaturation (S_c) ranged from 20 cm^{-3} (pristine) to 350 cm^{-3} (anthropogenic) with an average of 106 ± 54 cm^{-3} over the experiment. The inferred supersaturation in the clouds sampled during this experiment is $\sim$0.3%. CCN concentrations of cloud-processed aerosol were well predicted using an ammonium sulfate approximation for $S_c \leq 0.4\%$. Predicted N_{CCN} for other aerosol types (i.e., Asian and North American aerosols) were high compared to measured values indicating a less CCN active aerosol. This study highlights the importance of chemical effects on CCN measurements and introduces a CCN activation index as a method of classifying the efficiency of an aerosol to serve as CCN relative to an ammonium sulfate particle. This index ranged from close to unity for cloud processed aerosols to as low as 0.31 for aged aerosols transported from Asia. We also compare the performance of two CCN instruments (static thermal diffusion chamber and streamwise continuous flow chamber) on a 45 minute level leg where we observe an aged layer and a nucleation event. More than 50% of the aged aerosol served as CCN at 0.2% S_c, primarily owing to their large size, while CCN concentrations during the nucleation event were close to 0 cm^{-3}. CCN concentrations from both instruments agreed within instrument errors; however, the continuous flow chamber effectively captured the rapid transition in aerosol properties.

Citation: Roberts, G., G. Mauger, O. Hadley, and V. Ramanathan (2006), North American and Asian aerosols over the eastern Pacific Ocean and their role in regulating cloud condensation nuclei, *J. Geophys. Res.*, *111*, D13205, doi:10.1029/2005JD006661.

1. Introduction

[2] Dust and anthropogenic emissions from Asia traverse the Pacific Ocean and intercept the North American continent within several days during the spring months when storm and frontal activity is most intense. Numerous field campaigns, i.e., ACE-Asia [*Seinfeld et al.*, 2004], APEX [*Sano et al.*, 2003] and INDOEX [*Ramanathan et al.*, 2001], have documented the direct impact of the long-range transport of dust and anthropogenic emissions on radiative fluxes to the surface. Since dust and biomass burning aerosols also provide surface area for the uptake of gas-phase species (i.e., sulfates and nitrates), over time these aerosols become more hygroscopic and may play an important role in cloud formation during their transport. Cloud droplet concentrations, cloud depth and liquid water content determine the albedo of stratocumulus clouds [*Twomey*,

[1]Center for Atmospheric Sciences, Scripps Institution of Oceanography, La Jolla, California, USA.

0148-0227/06/2005JD006661$09.00

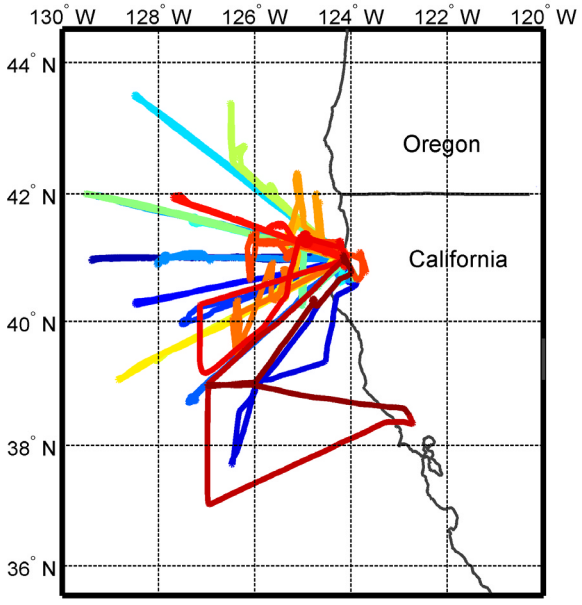

Figure 1. Flight tracks during the CIFEX experiment used for the CCN analysis. Flight operations were based out of the Eureka/Arcata Airport at 40°58.687′N/124°06.517′W.

1977] which extend over large regions of the Pacific Ocean and strongly influence solar energy input into the Earth-atmosphere system. Droplet concentrations in cumulus clouds are largely controlled by the physicochemical properties of aerosol and updraft velocity at cloud base [*Twomey and Warner*, 1967; *Seinfeld and Pandis*, 1998]. A significant fraction of the aerosol in the eastern Pacific originates from anthropogenic activity; hence, it is important to identify the aerosols capable of nucleating into clouds drops. This subset of aerosol is known as cloud condensation nuclei (CCN). The CCN spectrum relates the concentration of CCN (N_{CCN}) to a range of supersaturations (S_c) and to derive cloud droplet concentrations (n_D) for a prescribed updraft velocity in climate models [*Twomey and Squires*, 1959; *Feingold and Heymsfield*, 1992; *Roberts et al.*, 2003]. Previous studies have shown that N_{CCN} (S_c < 1%) are typically lowest ($N_{CCN,1.0}$ < 200 cm^{-3}) in the unpolluted marine atmosphere [*Hegg et al.*, 1991; *Hudson*, 1993; *Covert et al.*, 1998; *VanReken et al.*, 2003] and highest ($N_{CCN,1.0}$ > 10^3 cm^{-3}) in regions influenced by anthropogenic sources [*Hudson*, 1991; *Ramanathan et al.*, 2001; *Roberts et al.*, 2002; *VanReken et al.*, 2003].

[3] CCN concentrations can be accurately predicted on the basis of known aerosol size distributions and chemical composition according to Köhler theory [*Köhler*, 1936; *Seinfeld and Pandis*, 1998]. Several studies [*Bigg*, 1986; *Covert et al.*, 1998; *Chuang et al.*, 2000; *Roberts et al.*, 2002; *VanReken et al.*, 2003] have investigated aerosol-CCN closure with considerably different results. In this study, we focus on simultaneous measurements of CCN and aerosol size distributions to determine if closure can be achieved without explicit size-resolved chemical measurements. A comparison of the aerosol size distributions to the measured CCN concentration provides insight to the chemical evolution of the aerosols and their potential effect on aerosol/cloud interactions during long-range transport.

[4] The Cloud Indirect Forcing Experiment (CIFEX; http://borneo.ucsd.edu/cifex), in April 2004, focused on the measurement of aerosol and cloud properties to assess the impact of long-range transport on aerosol-cloud interactions. As a pilot study for the Atmospheric Brown Cloud project, CIFEX allows a comparison to the aerosol-CCN-cloud interactions in the polluted N. Indian Ocean [*Ramanathan et al.*, 2001], which is influenced by long-range transport from India and southwest Asia. In the CIFEX study, we present airborne measurements obtained onboard the University of Wyoming King Air, a twin turboprop aircraft equipped for tropospheric measurements. The experiment operated from the Eureka/Arcata airport in Northern California (near the Trinidad Head site operated by the NOAA Climate Monitoring and Diagnostics Laboratory; CMDL), where we expected to intercept plumes of pollution and dust transported from the Asian continent across the Pacific Ocean. During the CIFEX experiment, the King Air aircraft flew 24 research missions characterizing aerosol and cloud properties off the coast of California (up to 500 km from the coast) and between 500 and 7500 m above sea level (asl). Figure 1 shows the 23 flight tracks where CCN measurements are available, and Table 1 provides details on each research flight (i.e., date/time, flight duration, type of mission, type of CCN measurements). Section 3 describes the six aerosol classes shown in Table 1. Section 4 then correlates the aerosol types to CCN measurements to provide insight on their efficiency to serve as CCN. The analysis concludes in section 5 with a case study of aerosol properties and how a transformation in aerosols affects CCN measurements.

2. Instrumentation

[5] The King Air payload for aerosol and cloud measurements is shown in Table 2. Airborne measurements include aerosol number concentration and size distribution (N_{CN} and $n(D_p)$, respectively), CCN concentrations (N_{CCN}), cloud number concentrations and size distributions (n_D and $n_D(D_p)$, respectively), and aerosol back scattering (σ_b). Two CCN counters were operated during the experiment; a static thermal gradient chamber [*Snider and Brenguier*, 2000] and a continuous flow streamwise thermal gradient chamber [*Roberts and Nenes*, 2005], and are described in sections 2.1 and 2.2, respectively.

[6] Measurements of N_{CN} were performed with a condensation nuclei counter (CPC 3760; TSI Inc., St. Paul, Minnesota). Aerosol size distributions were measured by a scanning mobility particle sizer (SMPS 3081; TSI Inc., St. Paul, Minnesota) from 0.01 < D_p < 0.4 μm at a rate of one distribution every 50 s. Section 2.3 describes corrections to the SMPS transfer functions. A wing-mounted Particle Measuring Systems PCASP-100X (PMS Inc., Boulder, Colorado) optical particle counter measured the aerosol size distribution from 0.2 < D_p < 3 μm. The PCASP was calibrated using polystyrene latex spheres (index of refraction; n = 1.586) and has been corrected to equivalent scattering spheres at n = 1.45 [*Liu and Daum*, 2000]. The SMPS and PCASP distributions are combined to yield aerosol distributions from 0.01 to 3 μm diameter. Aerosol sampled by the CN, SMPS, and CCN counters entered the King Air via a forward facing shrouded diffuser-type inlet. The diffuser has

Table 1. Summary of King Air Missions for CIFEX[a]

Flight Number	Day of Year	Launch Date/Time, UTC	Flight Duration, hours:min	Aerosol Classification	CCN Data S_c, %
2	93	2 April, 21:51	3:12	*NA*, *NA*, *NA*	0.2, 0.4, 0.6[b]
3	94	3 April, 17:52	3:14	*NA*, *NA*, *NA*	0.3[b]
4	94	3 April, 0:21	3:14	*NA*, L_{trans}, L_{fine},*NA*	0.3[b]
5	96	5 April, 15:56	3:11	*P*, *P*	0.3[b]
6	96	5 April, 21:31	3:23	*P*, *P*, *P*	0.3[b]
7	97	6 April, 15:53	3:36	*P*, L_{trans}, *P*, *NA*	0.3[b]
8	98	7 April, 13:55	3:07	*P*, L_{trans}, *P*	0.3[b]
9	98	7 April, 18:14	3:36	L_{trans}, L_{trans}, L_{fine}, L_{trans}	0.3[b]
10	100	9 April, 15:21	4:04	*NA*, L_{aged}, L_{aged}, L_{fine}, *NA*	0.3[b]
11	100	9 April, 21:36	4:04	*NA*, L_{trans}, L_{aged}, L_{fine}	0.3[b]
12	101	10 April, 17:06	3:43	*NA*, L_{trans}, L_{trans},*NA*,*NA*	0.2, 0.4, 0.6[b]
13	103	12 April, 16:04	3:36	*P*, *P*	0.2, 0.4, 0.6[b]
14	104	13 April, 16:55	3:43	*P*	0.2, 0.4, 0.8[b]
15	105	14 April, 17:14	3:23	L_{fine}, L_{aged}, L_{fine}, L_{fine}	0.2, 0.4, 0.8[b] 0.2[c]
16	105	14 April, 21:59	3:36	*P*, *P*	0.2, 0.4, 0.8[b]
17	106	15 April, 18:46	3:48	*P*, *P*	0.2, 0.4, 0.8[b] 0.2[c]
18	108	17 April, 18:05	3:30	*P*	0.2, 0.4, 0.8[b]0.2[c]
19	108	17 April, 22:48	3:36	*P*	0.2, 0.4, 0.8[b]
20	109	18 April, 19:12	4:04	*P*	0.2, 0.4, 0.8[b]
21	111	20 April, 12:56	3:50	L_{aged}, *P*, *M*	0.2, 0.4, 0.8[b]
22	111	20 April, 18:54	4:04	L_{trans}	0.2, 0.4, 0.8[b]
23	112	21 April, 14:57	3:31	*P*, L_{aged}	0.2, 0.4, 0.8[b]
24	112	21 April, 20:03	3:25	*P*, *M*, *P*	0.2, 0.4, 0.8[b]

[a]Aerosol classifications are separated into the following categories: *M*, marine boundary layer; *P*, cloud processed aerosol; *NA*, North American continental; L_{fine}, ultra-fine recent new particle formation; L_{trans}, transitional long-range transport; and L_{aged}, aged aerosol layers.
[b]Static thermal gradient CCN instrument (STG-CCN).
[c]Continuous flow streamwise thermal gradient CCN instrument (CFS-CCN).

an expansion angle of 6 degrees with an expansion ratio of ~25 and sampled quasi-isokinetically by decelerating the air speed from 90 m s^{-1} to 3.5 m s^{-1}. Calculations based on impaction theory [*Foltescu et al.*, 1995] indicate the D_{50} cut size is ~8 μm, but have not been experimentally characterized. The results presented in this paper are not sensitive to the exact cut-size diameters as the number concentration of supermicron particles is small compared to the CCN-sized submicron fraction. The CN, SMPS, and CCN instruments were located inside the cabin of the King Air where they operated at least 15°C higher than outside ambient temperatures. Therefore we assume most water evaporated prior to detection. Meteorological data measurements such as temperature, pressure, and relative humidity were also measured. Specific details on the University of Wyoming King Air facility instruments are described at http://flights.uwyo.edu.

2.1. Static Thermal Gradient CCN Instrument

[7] The University of Wyoming CCN instrument (STG-CCN) is similar to other static thermal gradient chambers [*Twomey*, 1963; *Lala and Jiusto*, 1977] and measures CCN concentrations once every 40 s at a particular supersaturation. The CCN chamber operated in single supersaturation mode (S_c = 0.3%) from flights 3 to 11 and CCN spectra mode (one CCN spectrum every 120 s; 0.2, 0.4 and 0.6 or 0.8% S_c) for all other flights (Table 1). A CCN cycle begins with a purge to remove the previous sample and draw in air for a new sample. The instrument's inlet valve closes and isolates the chamber, which allows the supersaturation profile to develop between two horizontal parallel wetted plates. Activated CCN particles quickly grow to several micrometers in diameter and gravitationally settle out of the chamber. A 670-nm laser diode illuminates droplets as they grow while a photodetector measures the amount of scattered light. The voltages are recorded continuously at 1 Hz. The processing of the STG-CCN data had several levels of quality control and the data was rejected if the following conditions were encountered: (1) the peak voltage from the detector did not exceed two standard deviations from the noise in the base voltage; (2) the base voltage changed by more than a predetermined amount during the detection cycle; and (3) peaks were below a certain threshold. Counting errors become a significant source of uncertainty at low concentrations (±30% at 30 cm^{-3}; the lower detection limit for N_{CCN} of the STG-CCN). The error associated with the number concentrations from the STG-CCN chamber are expected to be within 40% [*Snider and Brenguier*, 2000; *Nenes et al.*, 2001].

Table 2. King Air Instrument Payload During CIFEX

Instrument	Measurement	Sample Rate, s
Condensation particle counter (CPC 3760; TSI)	concentration (N_{CN}; D_p > 10 nm)	1
Scanning mobility particle sizer (SMPS; TSI)	size distribution (n(D_p); 10 < D_p < 400 nm)	50
Passive cavity aerosol spectrometer probe (PCASP-100X; PMS)	size distribution (n(D_p); 0.2 < D_p < 3 μm)	1
Integrating nephelometer (Radiance Research)	hemispherical scattering (σ_b; λ = 530 nm)	1
Static thermal gradient CCN Counter (Univ. Wyoming)	concentration (N_{CCN}; 0.2, 0.3, 0.4, 0.6, 0.8% S_c)	~40 s S_c^{-1}
Continuous flow streamwise CCN Counter (DMT)	concentration (N_{CCN}; 0.2% S_c)	1
Forward scattering spectrometer probe (FSSP-100; PMS/DMT)	size distribution (n_D (D_p); 1 < D_p < 45 μm)	1

[8] The STG-CCN counter operates at a desired supersaturation by controlling the temperature difference between the wetted plates and its calibration consists of introducing a monodisperse sample of known composition with size greater than the critical activation size using a differential mobility analyzer (DMA). The performance of the STG-CCN is measured at several different concentrations and several different supersaturations. The aerosol stream is simultaneously sampled by a CPC, and the calibration consists of fitting the peak voltage from the detector to the number concentration from the CN. The supersaturation is calibrated from Köhler Theory by using the D_{50} of the activation curve. Details of the calibration procedures are discussed by *Delene et al.* [1998], *Snider and Brenguier* [2000] and *Bilde and Svenningsson* [2004].

2.2. Continuous Flow Streamwise CCN Instrument

[9] The continuous flow streamwise thermal gradient CCN instrument (CFS-CCN) exploits the differences in diffusion between water vapor and heat to maintain a quasi-uniform supersaturation along the streamwise axis of the chamber [*Roberts and Nenes*, 2005]. A vertical cylindrical column, whose surfaces are wetted and exposed to an increasing temperature gradient along the vertical axis, constitutes the growth chamber. An air sample is introduced at the center of the column and is surrounded by an aerosol-free humidified sheath flow to keep the sample in a region of nearly uniform supersaturation and minimize wall losses. The air then flows vertically downward through the chamber, where CCN activate and grow into droplets. An optical particle counter at the outlet of the chamber counts droplets with diameters larger than 0.5 μm. Those droplets larger than 1 μm are considered activated CCN and comprise the CCN concentration.

[10] These flights were the first airborne flights for the CFS-CCN manufactured by Droplet Measurement Technologies (Droplet Measurements Technologies; Boulder, Colorado). The CFS-CCN operated at 500 cm^3 min^{-1} and a temperature difference of 4.22°C between the ends of the column. The air flow and temperature gradient control the supersaturation are maintained within 5% of the desired values. Under such conditions, instrument calibrations conducted prior to the CIFEX experiment at 825 mbar showed that $(NH_4)_2SO_4$ aerosol activated at $D_{50,dry}$ = 74 nm, corresponding to 0.22% S_c using Köhler theory. Variations in pressure exert second-order changes in supersaturation (~0.03% S_c per 100 mbar [*Roberts and Nenes*, 2005]); therefore small corrections to the operating supersaturation must be applied for airborne operation. For this study, we focus on CFS-CCN measurements from a horizontal flight at 700 mbar, resulting in a supersaturation of 0.19% S_c and compare these measurements to those of the STG-CCN instrument at 0.2% S_c (sections 4 and 5). The error associated with the number concentrations from the CFS-CCN chamber are less than 10% [*Roberts and Nenes*, 2005]. At low number concentrations (<60 cm^{-3}), counting statistics become important. Most of the 1-σ standard deviations presented here are associated to variations in number concentrations.

2.3. Scanning Mobility Particle Sizer

[11] The scanning mobility particle sizer (SMPS) effectively measured size and number of particles between 0.01 and 0.4 μm with a resolution of 14 channels per decade. Size distributions were obtained every 50 s during each up and down scan and have been corrected to account for pressure and temperature changes during flights. The algorithms for inverting data employing continuous voltage scanning are described by *Wang and Flagan* [1990] and include multiple charge corrections and the calculation of the mean free path with respect to pressure and temperature changes. Additional corrections include diffusional broadening [*Zhang and Flagan*, 1996] and desmearing of the CN data [*Collins et al.*, 2002]. The inverted size distribution are not smoothed for the present analysis. The routines have been written using MatLab and process the raw output data files from TSI Corporation's Aerosol Instrument Measurements Software (AIMS).

3. Airborne Measurements During CIFEX

[12] The King Air flights measured physical properties of aerosols and clouds over the eastern Pacific Ocean (Figure 1). The air sampled during the campaign varied considerably, ranging from pristine conditions ($N_{CN} < 10^2$ cm^{-3}) to distinct anthropogenic influence ($N_{CN} > 10^4$ cm^{-3}). The first several flight missions have a distinct aerosol focus as a large anticyclone circulation carried continental aerosol from North America westward over the ocean where this anthropogenic haze was observed up to several hundred kilometers from shore and confined to the marine boundary layer (i.e., altitudes less than 2000 m asl). Aerosol layers above the marine boundary layer frequently exhibit Asian origins as indicated by back trajectories [*Draxler and Hess*, 1997] and take between 3 and 5 days to travel across the Pacific Ocean and transect the coast of North America. A variety of cloud systems were observed throughout the experiment including low-level stratocumulus and mixed-phase or ice clouds up to 5 km. In-cloud aerosol data have been removed as droplet shattering on the aerosol inlet biases aerosol concentrations and size distributions.

3.1. Vertical Structure of Aerosols

[13] An ensemble average of vertical profiles over the eastern Pacific Ocean during the CIFEX experiment is shown in Figure 2. Only measurements taken more than 50 km from the North American coast are shown to minimize the sampling bias of land-sea breeze circulation which could carry aerosols from Humboldt County, California, over the ocean. This step is precautionary as *VanCuren et al.* [2005] report that marine aerosols at Trinidad Head, California, generally dominate the chemical composition with varying minor contributions from local sources. The number of measurements at a particular altitude is shown on the right axes of the subplots in Figure 2; most of the observations were between 500 and 4500 m asl. Only one flight (Flight 22) measured aerosols above 6000 m asl. Measurements are considered part of a vertical profile under the following conditions: (1) the ascent/descent rate is between 1 and 5.1 m s^{-1}; (2) the elevation difference between the start and end of the profile is greater than 1000 m; (3) ascents/descents joined by a level leg less than 120 s; and (4) the profile is greater than 50 km from the coast.

[14] Aerosol concentrations (N_{CN}) averaged 630 cm^{-3} in the marine boundary layer (average height ~1200 m asl)

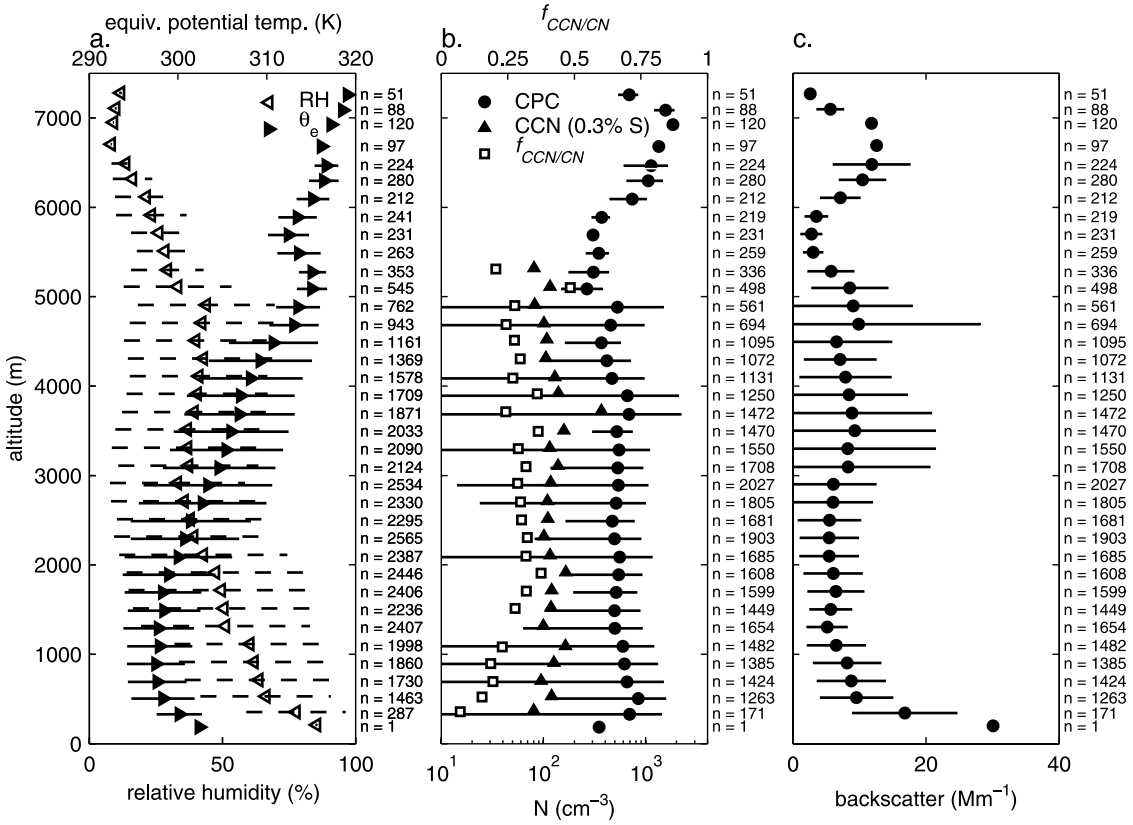

Figure 2. Average vertical profile using data from all flights for (a) equivalent potential temperature and relative humidity, (b) N_{CN}, $N_{CCN,0.3}$, $f_{CCN/CN}$, and (c) backscatter. One sigma error bars are shown for all data except N_{CCN} and $f_{CCN/CN}$. The number of samples at a given altitude is shown on the right axis of each plot.

and 500 cm^{-3} between 1200 and 5000 m (Figure 2b). Large variability in N_{CN} below 1200 m was observed as clean ($N_{CN} \sim 10^2$ cm^{-3}) and polluted ($N_{CN} \geq 10^3$ cm^{-3}) conditions (regional aerosol from North America) were sampled in the offshore boundary layer. Standard deviations are reported as one sigma values throughout this analysis. The observed concentration of aerosol above the marine boundary layer ($N_{CN} \sim 500$ cm^{-3}) is higher than the global average of 250 cm^{-3} [*Jaenicke*, 1992; *Seinfeld and Pandis*, 1998] because of frequent observations of new particle formation and the input of long-range transport. We observed long-range transport from Asia primarily between 2000 and 5000 m as indicated by the large variability in N_{CN} ($D_p > 10$ nm; Figure 2b), backscatter (σ_b) measurements ($\lambda = 530$ nm; Figure 2c) and back trajectories. Distinct aerosol layers were also observed as high as 7200 m (Flight 22) with N_{CN} and σ_b aloft exceeding 10^3 cm^{-3} and 10 Mm^{-1}, respectively. CCN concentrations (0.3% S_c; STG-CCN) averaged 125 cm^{-3} with an activated fraction ($f_{CCN/CN}$) of 0.3 in the free troposphere and decreasing in the boundary layer to less than 0.1. The decrease of $f_{CCN/CN}$ in the boundary layer is a result of the large number of small, less CCN-active aerosols from North American anthropogenic emissions.

[15] Throughout the experiment, we observed large-scale subsidence as observed from the increasing equivalent potential temperature above the marine boundary layer (Figure 2a). This atmospheric stability stratifies and preserves the structure of the aerosol layers in the free troposphere. Occasional storm fronts provide vigorous vertical mixing between the marine boundary layer and free troposphere up to 5000 m during the CIFEX. *Van Dingenen et al.* [1999] conclude that the entrainment of free tropospheric air into the boundary layer is the most important process controlling the relationship between the sulphate mass and CCN available for cloud formation over the ocean. These conclusions are also supported by measurements at the NOAA CMDL Trinidad Head site during the Intercontinental Transport and Chemical Transformation 2002 (ITCI 2K2) experiment as *VanCuren et al.* [2005] observed that even in the presence of Asian continental aerosol above the marine boundary layer, significant contributions of Asian aerosols were observed at the ground only during a strong frontal passage. Therefore the extent of this vertical mixing determines the potential impact of the long-range Asian transport on the aerosol indirect effect and needs further investigation.

3.2. Aerosol Classification

[16] Six aerosol types were identified during CIFEX (Figure 3) on the basis of distinguishing features of the size distribution (i.e., median diameter, number concentration, number of modes) and 5-day back trajectories which indicate the origin of the air mass. Back trajectories were computed using HYSPLIT [*Draxler and Hess*, 1997] and three examples characteristic of back trajectories during the

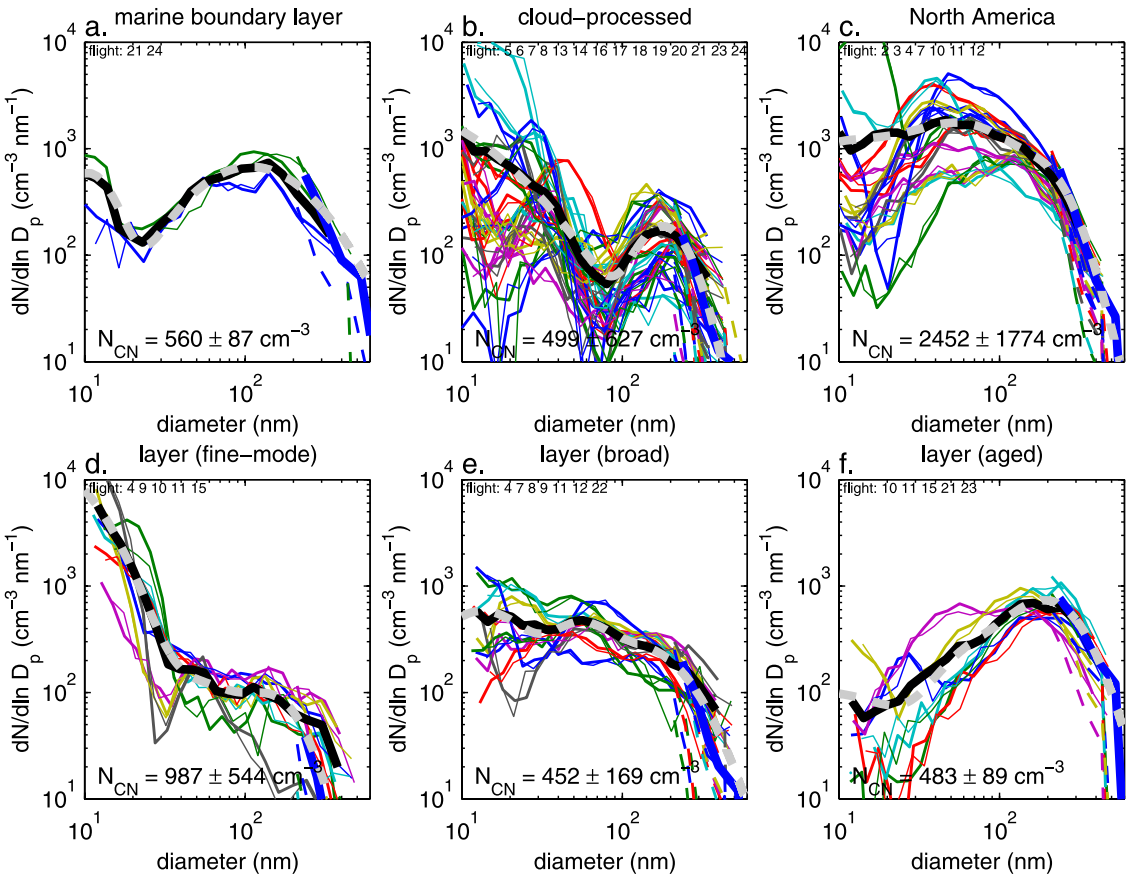

Figure 3. Aerosol classification based on size distributions and back trajectories. Average distributions for SMPS and PCASP measurements are shown in thick black and blue lines, respectively. Thick dashed lines show the lognormal approximations. Average $N_{CN} \pm 1$ σ for each aerosol classification are also shown. Flight numbers in which size distributions were measured are specified in the upper left of each plot.

CIFEX are shown in Figure 4. The main aerosol types are (type a) marine boundary layer, (type b) recently cloud-processed, (type c) continental aerosol from North America, and (types d–f) three aerosol types associated with long-range transport from Asia. The cloud-processed size distributions (Figure 3b) are common near nonprecipitating clouds in the marine boundary layer and are identified by a trough between 60 and 80 nm [*Hoppel et al.*, 1986; *Garrett and Hobbs*, 1995]. Cloud processing is an efficient mechanism for accumulating sulfate mass for aerosols between $0.08 < D_p < 0.5$ μm in the remote marine atmosphere [*Hoppel et al.*, 1986; *Feingold and Kreidenweis*, 2002]. The total concentration of cloud-processed aerosol shows considerable variation ($\overline{N}_{CN} = 499 \pm 627$ cm^{-3}) because of the fluctuations in the concentration of particles $D_p < 60$ nm. The North American continental aerosol (Figure 3c) was identified by back trajectories which pass over the western coast of Canada and United States and carry regional anthropogenic emissions back out over the ocean (Figure 4b). These air masses from North America traveled between 6 and 24 hours over the ocean, exhibited significantly higher number concentrations ($\overline{N}_{CN} = 2450 \pm 1775$ cm^{-3}) and were sampled exclusively within the marine boundary layer. The aerosol number distributions from North America were monomodal, with maxima near 60 nm diameter. *Garrett and Hobbs* [1995] observed similar size distributions over the Atlantic Ocean for aerosols associated with transport of anthropogenic aerosols from Europe. During CIFEX, aerosol layers were often found above the marine boundary layer and were readily identified during vertical profiles by elevated concentrations compared to the free troposphere. Back trajectories corresponding to these layers aloft point to an Asian origin in which air masses traversed the Pacific Ocean in 4 to 6 days. Three categories of aerosols associated with long-range transport were identified as the size distributions in Figures 3d–3f show distinct differences. Large concentrations of ultrafine aerosols ($D_p < 30$ nm; L_{fine}; Figure 3d) indicate new particle formation has recently occurred. New particle production is common of Asian outflow in the West Pacific Ocean [*McNaughton et al.*, 2004] when postfrontal air masses enhanced the production of new particles by an order of magnitude. Their results from the Aerosol Characterization Experiment 2 (ACE-2) also show that scavenging of secondary aerosol in the marine boundary layer appears to be important as 10–30% of the aerosol consist of aged secondary aerosol after 2 days over the

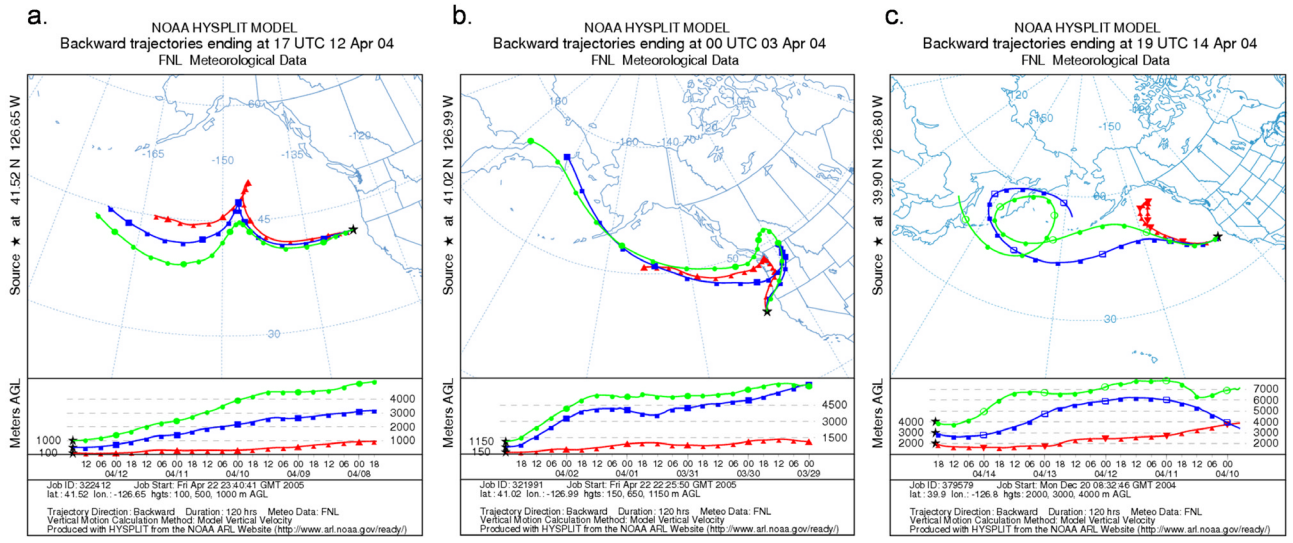

Figure 4. Example HYSPLIT back trajectories for (a) marine boundary layer aerosol, (b) North American continental aerosol, and (c) long-range transport aerosol from Asia.

ocean. Previous studies [*Weber et al.*, 2003; *McNaughton et al.*, 2004] have estimated new particle growth rates of $\sim$2 nm h^{-1} in marine environments; hence we expect a transition of aerosol size distributions from Figures 3d to 3e (L_{trans}) to occur on timescales of a day [*Raes et al.*, 2000]. Finally, the large mode (median $D_p \sim 200$ nm) in Figure 3f suggests an aged aerosol (L_{aged}; Table 1). The aged aerosol concentrations averaged 483 ± 89 cm^{-3} and were confined to layers above the boundary layer (between 2000 and 5000 m asl). These aerosols do not appear to have been involved in cloud processing as they lack a characteristic minimum. Sections 4 and 5 show that while they contain small amounts of soluble material, the aged aerosols readily serve as CCN because of their large size. Although no chemical measurements were taken to verify the source of the aged aerosol, the Chemical Weather Forecast System (CFORS) [*Uno et al.*, 2003] predicted the arrival of dust from the Asian continent.

[17] The measured aerosol size distributions have been approximated by multimodal lognormal distributions

$$\frac{dN}{d\ln D_p} = \sum_{m=1}^{n} \frac{N}{\ln\sigma\sqrt{2\pi}} \exp\left[\frac{-\left(\ln D_p - \ln D_{pg}\right)^2}{\ln^2\sigma}\right],$$

where N, σ and D_{pg} are the aerosol number concentration, geometric standard deviation, and median diameter for each mode m, respectively. Parameters for multimodal lognormal curves that best represent each aerosol classification are shown in Table 3 and overlaid on Figures 3a–3f.

4. CCN Measurements

[18] Two types of CCN counters were on board the King Air during the CIFEX experiment; the static thermal gradient CCN instrument (STG-CCN) and continuous flow streamwise thermal gradient CCN instrument (CFS-CCN) and are described in section 2. The STG-CCN operated at several supersaturations, between 0.2% and 0.8% S_c and provided most of the data used in this study. The CFS-CCN operated at a fixed supersaturation, 0.2% S_c; however, because of mechanical issues, only data from three research flights are available. Table 1 summarizes the measurements from each CCN instrument during the CIFEX experiment.

[19] To establish the validity of the CCN measurements, a particular flight leg on 14 April (section 5) provides an opportunity to compare the performance of the STG-CCN and CFS-CCN instruments. Figure 5 shows acceptable agreement between both CCN instruments at 0.2% S_c. The data were taken during the level portion of Flight 15 as described in section 5. As the STG-CCN collected CCN spectra and N_{CCN} was low for much of the leg, only 15 measurements are available for comparison. The slope of the best fit is 1.055 ($r^2 = 0.673$). While we cannot deduce any systematic differences between the instruments from this analysis, it is important to state that variability in number concentrations associated with the STG-CCN (15 measurements) is primarily instrumental (i.e., counting statistics and detection constraints), whereas 1-σ standard deviations in Figure 5 for the CFS-CCN instruments are associated with variations in number concentrations ($\sim$460 measurements). The lower supersaturation limits of both CCN instruments are 0.2% and 0.06% for the STG-CCN

Table 3. Lognormal Distributions for Aerosol Classifications

Classification	Mode	N, cm^{-3}	D_{pg}, nm	σ
Marine boundary layer	1	499.7	10.4	1.404
	2	1285	108.2	2.132
Cloud processed aerosol	1	8560	2.52	3.428
	2	155.6	180.7	1.413
North American continental	1	3185	12.5	2.962
	2	2132	64.43	1.892
	3	325.3	190.1	1.427
Ultra-fine recent new particle formation	1	18720	5.67	1.815
	2	189.1	50.5	1.901
	3	63.6	155.9	1.450
Transitional long-range transport	1	875.8	13.5	1.815
	2	329.2	53.7	1.470
	3	376.0	131.1	1.798
Aged aerosol layers	1	276.9	7.73	3.001
	2	322.3	78.3	1.670
	3	791.2	201.4	1.587

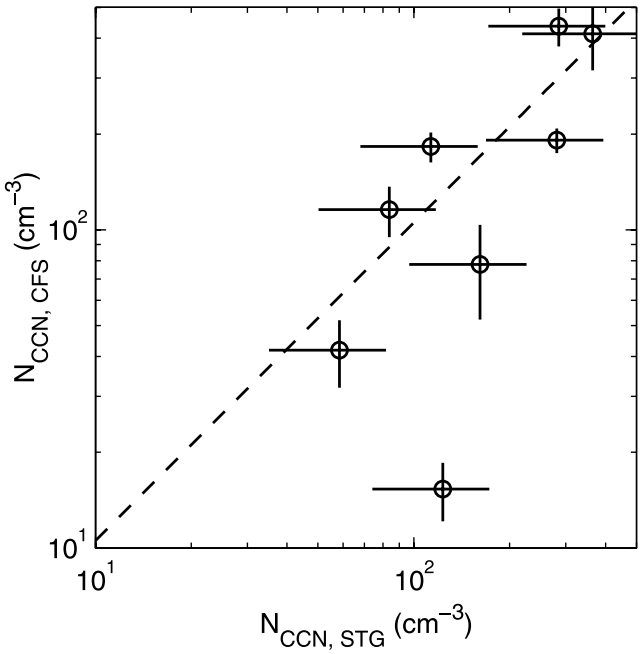

Figure 5. Measured CCN concentrations from both CCN instruments (0.2% S_c) during a level flight leg on 15 April 2004. The dashed line represents the 1:1 relationship.

and CFS-CCN, respectively [*Sinnarwalla and Alofs*, 1973; *Roberts and Nenes*, 2005]. The rest of this section reports results from the STG-CCN instrument. Measurements from both CCN instruments are discussed in section 5.

[20] Average CCN concentrations (for all measurements with the STG-CCN) observed during the CIFEX experiment at different supersaturations ($N_{CCN,Sc}$) are: $\overline{N}_{CCN,0.2}$ = 90 ± 54 cm^{-3}; $\overline{N}_{CCN,0.3}$ = 106 ± 54 cm^{-3}; $\overline{N}_{CCN,0.4}$ = 133 ± 96 cm^{-3}; $\overline{N}_{CCN,0.8}$ = 144 ± 118 cm^{-3}. Earlier studies have used the parameterization, $N_{CCN} = CS_c^k$ to describe CCN spectra [*Squires*, 1952; *Twomey and Squires*, 1959; *Pruppacher and Klett*, 1997]. For the purpose of comparison with previous results, the average values of C and k for the CIFEX study are 168 cm^{-3} and 0.38 ± 0.08, respectively. Maritime air masses generally exhibit values for C in the few hundreds cm^{-3} and k between 0.3 and 1.4 [*Pruppacher and Klett*, 1997, Table 9.1]. Aerosol size distributions and size-resolved chemical composition affect the C and k parameterizations and ultimately influence the ability to predict CCN concentrations.

[21] This section examines the ability to predict CCN concentrations on the basis of size distribution data without size-resolved measurements of aerosol composition and introduces a CCN activation index to classify the efficiency of an aerosol to serve as CCN compared to an ammonium sulfate approximation. The CCN measurements were averaged to match the timescale of individual size distributions from the SMPS. CCN concentrations at a particular supersaturation were predicted on the basis of aerosol size distributions and Köhler theory using an ammonium sulfate, $(NH_4)_2SO_4$, approximation because (1) previous studies have shown that much of the sulfate in the marine boundary layer has been neutralized to ammonium sulfate, $(NH_4)_2SO_4$ [*Kline et al.*, 2004] and (2) ammonium sulfate has been used to calibrate both CCN instruments. Therefore deviations between predicted and measured CCN concentrations provide insight on the implicit ability of aerosols to serve as CCN. In these calculations, we assume the surface tension is that of water, $(NH_4)_2SO_4$ fully dissociates, and the insoluble core (chemical constituents other than $(NH_4)_2SO_4$) is CCN inactive.

[22] A total of 1884 comparisons between $N_{CCN,measured}$ and $N_{CCN,predicted}$ over 23 flights are shown in Figure 6 for the STG-CCN measurements at S_c between 0.2 and 0.8%. A regression of this data yields a relationship $N_{CCN,measured} = N_{CCN,predicted}^{0.846\pm0.002}$ (r^2 = 0.604) and the ratio of measured to predicted N_{CCN} is 0.56 ± 0.4. Such a relationship does not accurately describe a CCN closure; however, it is consistent with our measurements that high CCN concentrations are more influenced by anthropogenic sources, which are less CCN active. While considerable variability is observed between $N_{CCN,measured}$ and $N_{CCN,predicted}$, the standard deviation about the mean ($\sigma n^{-0.5}$ = 0.01) is relatively small because of the large number of samples. Therefore random instrumental error of the STG-CCN instrument probably does not account for the systematic bias. Earlier studies [*Bigg*, 1986; *Covert et al.*, 1998; *Chuang et al.*, 2000; *Snider and Brenguier*, 2000; *Wood et al.*, 2000] have found that CCN concentrations are also overpredicted on the basis of assumed or inferred chemical composition. *VanReken et al.* [2003] also found an overprediction of CCN at 0.85% S_c compared to 0.2% S_c in a marine environment on the only flight leg in which anthropogenic aerosol were sampled during CRYSTAL-FACE. Only a few studies [*Liu et al.*, 1996; *Cantrell et al.*, 2000; *Roberts et al.*, 2002] appear to achieve CCN closure because size-resolved chemistry from filter samples was used to calculate the CCN spectra. There

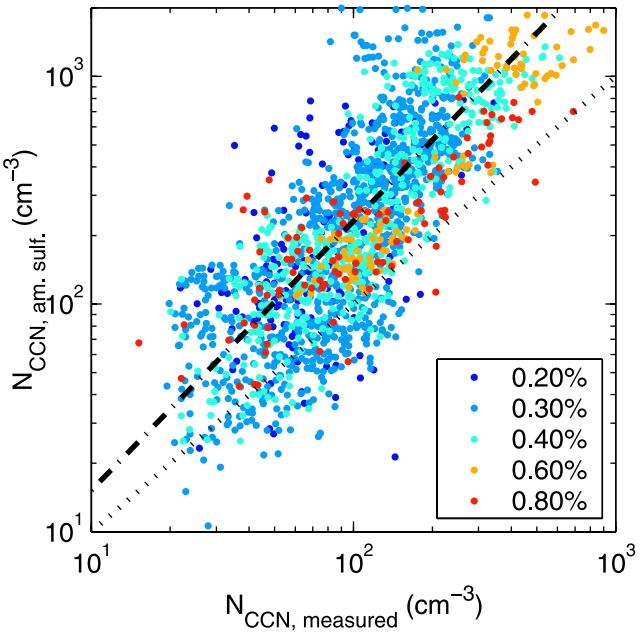

Figure 6. CCN closure at different supersaturations for all STG-CCN measurements using $(NH_4)_2SO_4$ and measured aerosol size distributions to calculated $N_{CCN,predicted}$. The dashed line shows the best fit, while the dotted line represents the 1:1 relationship.

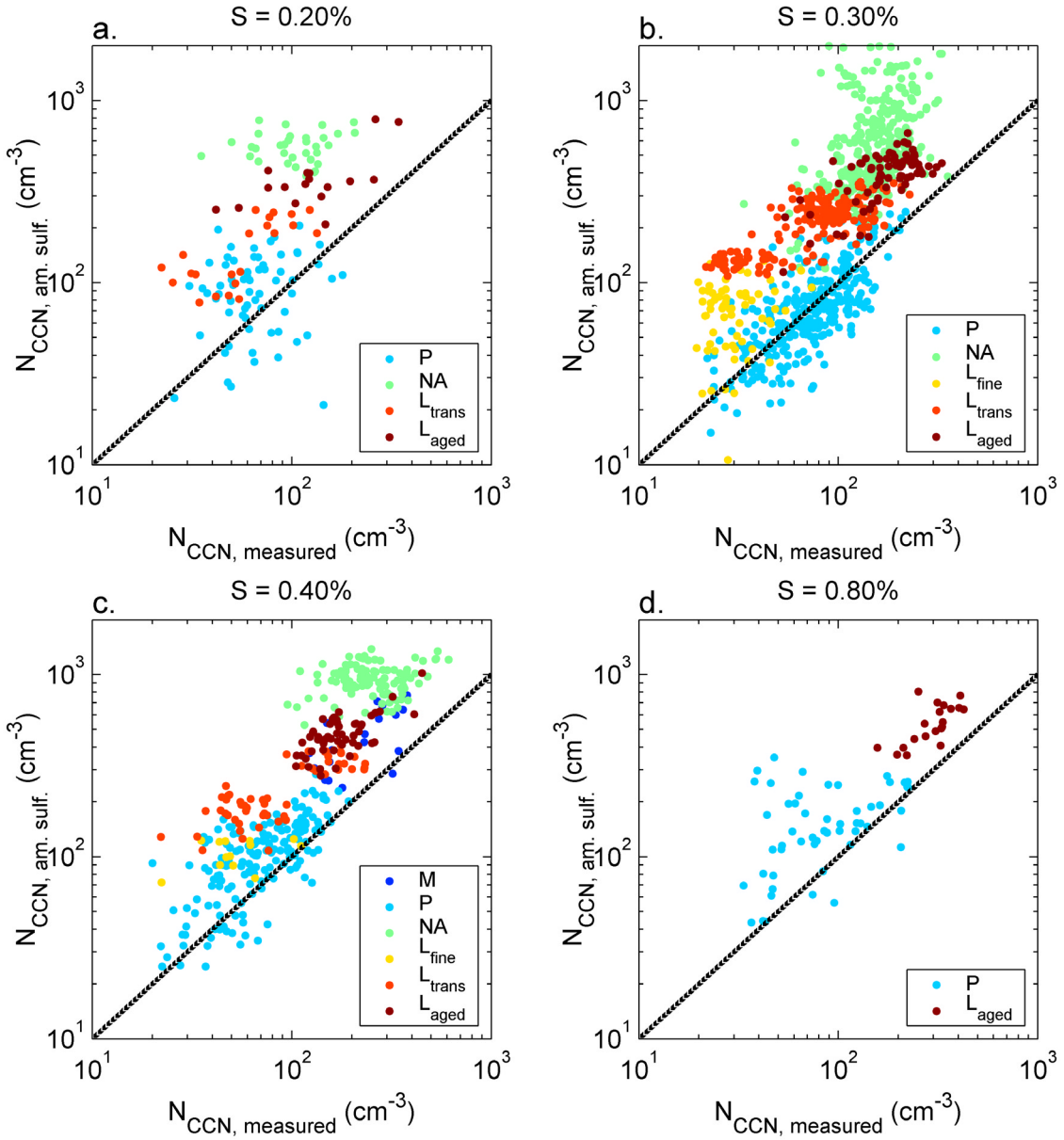

Figure 7. CCN closure (STG-CCN) for different aerosol classified as marine boundary layer, recently cloud processed, North American continental, and long-range transport based on $(NH_4)_2SO_4$ aerosol. See Figure 3 and section 3.2 for more details on the aerosol classification. The dotted line represents the 1:1 relationship.

are several possible explanations for the observed over-predictions of N_{CCN} during CIFEX including competition for water vapor, STG-CCN counting biases, delayed droplet growth due to organic coatings, and differences in chemistry for the aerosols sampled. Comparisons between the STG-CCN and CFS-CCN (previous section) indicate there is significant agreement at 0.2% S_c near the lower operational limit of the STG-CCN. STG-CCN and CFS-CCN chambers

Table 4. Ratio of Predicted to Measured N_{CCN} for Each Aerosol Classification and Supersaturation

	Supersaturation			
Classification	0.2%	0.3%	0.4%	0.8%
Marine boundary layer	...	...	2.06 ± 0.65	...
Cloud processed aerosol	1.54 ± 0.84 0.90	1.05 ± 0.43	1.52 ± 0.62	2.10 ± 1.60
North American continental	5.91 ± 2.77	4.28 ± 2.80	4.09 ± 1.57	...
Ultra-fine recent new particle formation	...	2.34 ± 1.14	2.11 ± 0.76	...
Transitional long-range transport	2.76 ± 1.07	3.00 ± 1.11	2.80 ± 1.06	...
Aged aerosol layers	3.16 ± 1.34	2.32 ± 0.72	2.74 ± 0.64	1.86 ± 0.42

Table 5. CCN Activation Index ($D_{pc,(NH4)2SO4}/D_{pc,measured}$) for STG-CCN Measurements at Each Supersaturation and Aerosol Type

Classification	Supersaturation			
	0.2%	0.3%	0.4%	0.8%
marine boundary layer	...	...	0.46 ± 0.23	...
cloud processed aerosol	1.02 ± 0.94	1.05 ± 0.53	0.60 ± 0.41	0.60 ± 0.31
North American continental	0.44 ± 0.09	0.40 ± 0.08	0.39 ± 0.10	...
ultra-fine recent new particle formation	...	0.59 ± 0.35	0.45 ± 0.23	...
transitional long-range transport	0.51 ± 0.11	0.40 ± 0.12	0.47 ± 0.15	...
aged aerosol layers	0.41 ± 0.11	0.31 ± 0.09	0.33 ± 0.08	0.32 ± 0.11

do not experience significant water vapor depletion for the CCN concentrations observed during CIFEX (N_{CCN} < 2000 cm^{-3}) [*Delene et al.*, 1998; *Roberts*, 2001; *Roberts and Nenes*, 2005].

[23] The systematic differences may originate from differences in aerosol chemistry. Hence, to extend the closure analysis further, aerosol size distributions have been separated according to their features and air mass history (Table 1 and section 3). Aerosol size distributions that exhibit different shapes have unique histories associated with different chemical signatures that are implicit to CCN measurements. Figure 7 shows the results of an aerosol-CCN closure based on the aerosol classification described in section 3 for each supersaturation. Different colors highlight clusters for each aerosol type. The cloud-processed cases (Figure 3a and Table 4) are closest to a 1:1 agreement between measured and predicted N_{CCN} at $\leq$0.4% S_c. Studies by *Kline et al.* [2004] show that marine boundary layer aerosols are neutralized as $(NH_4)_2SO_4$; hence the relatively good agreement between the predicted and measured CCN concentrations for cloud processed aerosol is expected. In contrast, Table 4 shows predicted N_{CCN} were 4 to 5 times that of measured N_{CCN} for aerosols associated with North American emissions and 2 to 3 times for long-range aerosol. This overprediction indicates a less CCN active aerosol: Either they have less soluble mass or hydrophobic material on the surface which inhibits droplet growth. *Shaw and Lamb* [1999] experimentally determined mass and thermal accommodation coefficients to be ~0.06 and 0.7, respectively. Simulations of the STG-CCN instrument have shown that accommodation coefficients greater than 10^{-4} result in particles counted as CCN [*Cantrell et al.*, 2000]. In spite of the lack of chemical information, it is evident that aerosol chemistry is playing a role in the CCN measurements and their activity is dependent on the aerosol classification.

[24] To quantify the ability of each aerosol type to serve as CCN, we introduce a CCN activation index for STG-CCN measurements at each supersaturation (Table 5). The CCN activation index offers a relativistic comparison of the ability of a particle to serve as CCN by comparing an experimentally determined critical diameter to that of ammonium sulfate for a given supersaturation (i.e., $D_{pc,(NH4)2SO4}/D_{pc,measured}$). The integration of the aerosol size distribution (section 2) to a diameter at which the integrated number concentration equals the measured CCN concentration yields an experimentally determined critical diameter ($D_{pc,measured}$). Aerosols which have a diameter larger than D_{pc} will activate into cloud droplets. A critical diameter is calculated based on Köhler Theory for simple aerosol mixtures when the chemical composition and particle size are known. Therefore, when chemical information is not known, the ratio a known salt's D_{pc} (i.e., $(NH_4)_2SO_4$) to the experimentally-derived D_{pc} offers a relativistic comparison of the ability of an aerosol to serve as CCN. A CCN activation index of one implies the particle behaves as an $(NH_4)_2SO_4$ aerosol, while indices less than unity imply less CCN active aerosol. Ratios of 0.5 and 0.25 indicate an equivalent $(NH_4)_2SO_4$ mass of 10% and 1%, respectively. Table 5 shows that cloud processed aerosols at 0.2% and 0.3% S_c have ratios closest to unity supporting results from previous studies [e.g., *Kline et al.*, 2004; *Feingold and Kreidenweis*, 2002] that cloud processing increases the efficiency of an aerosol to

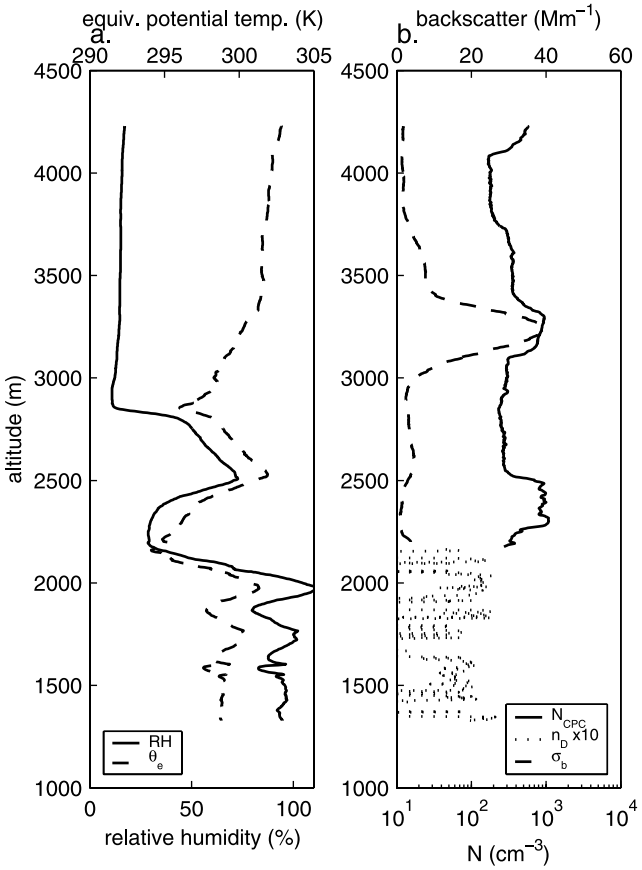

Figure 8. Vertical profile during Flight 15 (14 April 2004) of (a) equivalent potential temperature and relative humidity and (b) aerosol concentrations (N_{CN}), cloud drop concentrations (n_D), and hemispherical scattering (σ_b).

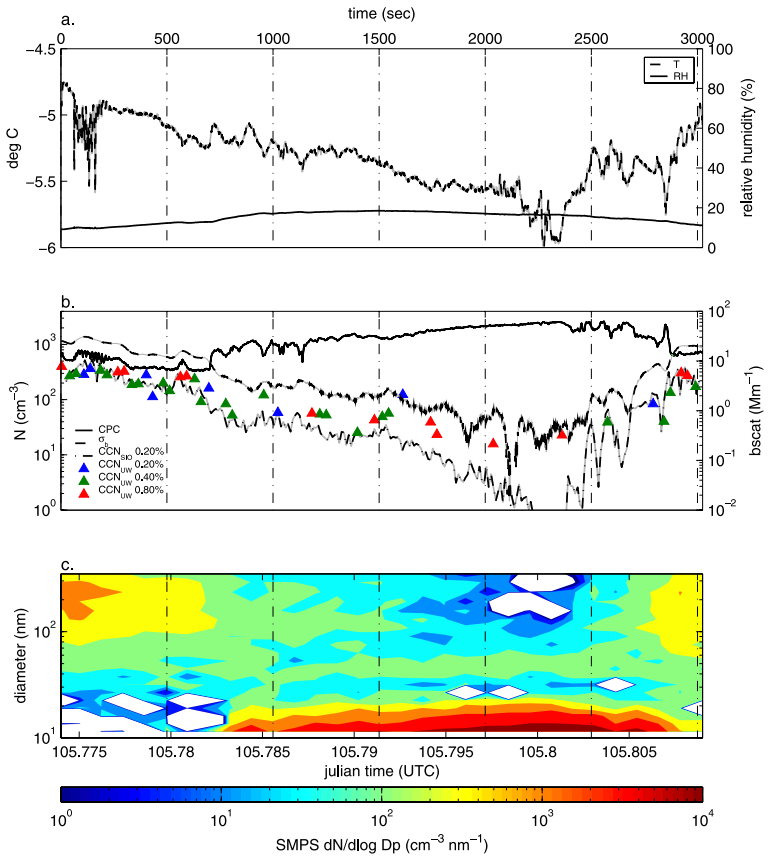

Figure 9. Time series during horizontal leg at 3100 m (Flight 15; 14 April 2004) of (a) temperature and relative humidity, (b) N_{CN}, N_{CCN}, σ_b, and (c) aerosol size distributions. Measurements from both CFS-CCN and STG-CCN instruments are shown.

serve as CCN. The other aerosol types in Table 5 have ratios less than 0.5 implying a less CCN active aerosol. The long-range, aged aerosol (L_{aged}) has the lowest CCN activation index suggesting a low soluble content, which is indicative of long-range transport of dust and biomass burning [*Gao et al.*, 1997; *Reid et al.*, 1998; *Zhang et al.*, 2003].

5. Case Study: Flight 15 (14 April 2004)

[25] While the previous sections present an ensemble analysis for the CIFEX experiment, this section focuses on Flight 15 (14 April 2005), which intercepted long-range transport of aged aerosol from Asia as shown by HYSPLIT back trajectories in Figure 4c. The back trajectories clearly indicate that dust and anthropogenic emissions from northern China traversed the Pacific Ocean in about four days. The trajectories also indicate that the marine boundary layer was decoupled from the free troposphere that carried the long-range transport. This study was characterized by a single stratocumulus layer about 700 m thick with its base at 1400 m asl. The aircraft ascended through the cloud, then followed a 45-min horizontal trajectory about 1000 m above cloud top. In this case study, we observed multiple aerosol layers in the vertical profile and a rapid transition of aerosol size distributions on a horizontal leg. The changes in aerosol properties effected CCN measurements in both CCN instruments.

5.1. Vertical Profile

[26] The vertical profile was taken at 40° 29.784 N/125° 29.064 W, 128 km northeast of the Eureka/Arcata airport. Two strong inversions (Figure 8a) and three aerosol layers (Figure 8b) characterized the vertical profile. Aerosol size distributions during the vertical profile (not shown) indicate that small particles (D_p < 50 nm) were dominant in two of these aerosol layers (at 2300 and 4100 m asl), probably a result of recent particle formation (Type L_{fine}; Figure 3d). While back trajectories suggest the aerosol layer at 4100 m asl may originate from Asian anthropogenic emissions, the vertical profile in Figure 8 points to a nucleation event near the cloud top in the 2300 m asl aerosol layer. Enhanced number concentrations near cloud tops have been observed in previous studies [e.g., *Hegg et al.*, 1990, 1991]. *Kerminen and Wexler* [1995] found that cool, moist, reduced surface area air masses above clouds are likely sites for new particle formation. The aerosol with median $D_p \sim$ 200 nm comprised the aerosol population at 3100 m asl, which is characteristic of aged aerosol (Type L_{aged}; Figure 3f); back trajectories also indicate an Asian origin. An inversion at 3000 m asl (Figure 8) decouples the marine boundary layer from this aged aerosol layer. Aerosol concentrations between the layers averaged 250 cm^{-3} and is similar to free tropospheric values of *Jaenicke* [1992] and *Seinfeld and Pandis* [1998].

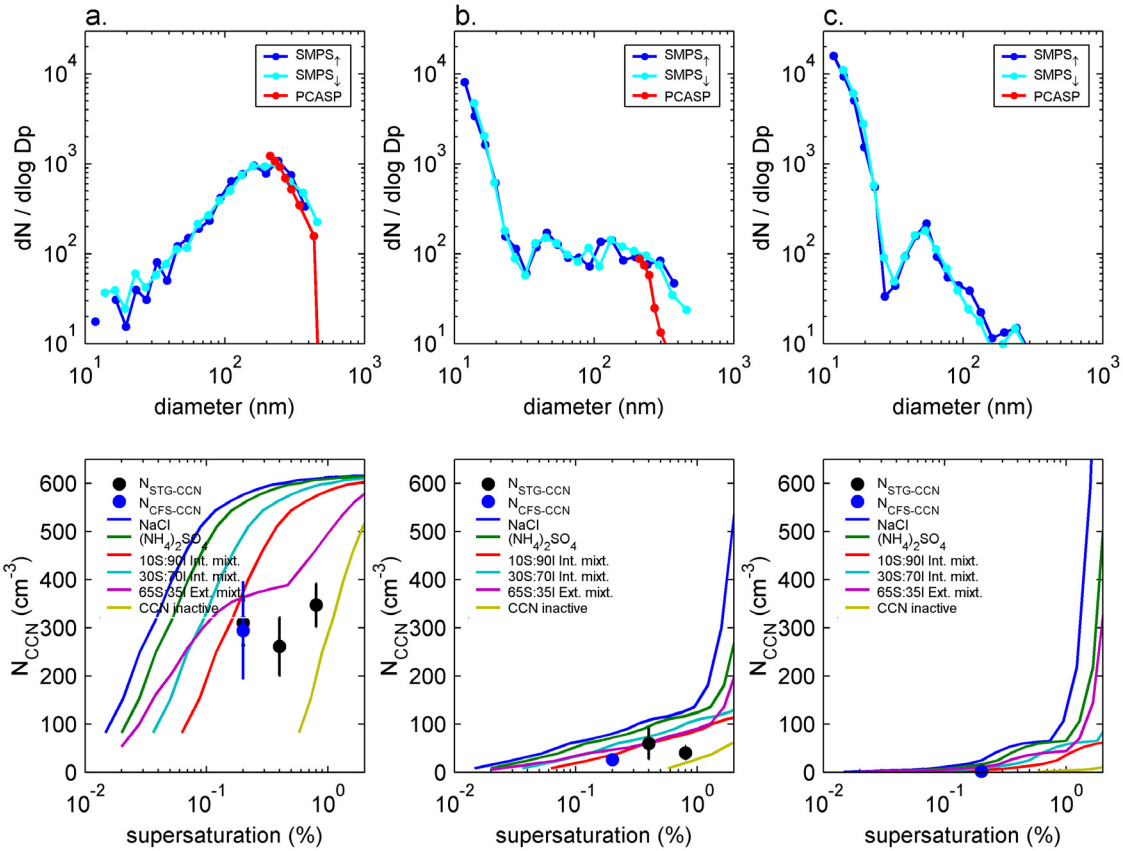

Figure 10. Average size distributions, calculated CCN spectra, and observed CCN concentrations for each period during the horizontal leg (15 April 2004).

5.2. Horizontal Transect

[27] The 45-min horizontal transect (Figure 9) begins in the aged aerosol layer at 3100 m asl. N_{CN} at the beginning of the leg averaged ~630 cm^{-3}; $N_{CCN,0.2}$ were also relatively high at ~350 cm^{-3} (Figure 9b). After 700 s into the leg, N_{CN} suddenly doubled, and then gradually increased to 2300 cm^{-3}, while N_{CCN} tapered to ~0 cm^{-3}. Aerosol backscatter measurements closely followed the trends of CCN. Aerosol size distributions in Figure 9c show changes consistent with observed trends of N_{CN}, N_{CCN} and σ_b. We have identified three periods of interest based on different aerosol size distributions (Figures 10a–10c): (1) aged mode (0–430 s); (2) ultra-fine and Aitken nuclei (865–1815 s); and (3) ultra-fine aerosols (1990–2420 s). The aged mode aerosol at the beginning of the leg was characterized by a large median D_p ~ 200 nm. The lack of a minimum between 60 and 80 nm diameter and ultra-fine particles (D_p < 20 nm) suggests the parcel had not undergone cloud processing or atmospheric mixing during its transport. An activation ratio ($f_{CCN/CN}$) of 0.54 at 0.2% S_c indicates that this aerosol can readily serve as CCN. The aged aerosol distribution quickly transformed to one with a large ultra-fine component mixed with Aitken nuclei as the relative humidity increased and sparse cloud cover changed to a precipitating stratus deck below as indicated by the Wyoming Cloud Radar (data not shown). The change in cloud properties below reflect a probable transition in vertical structure which induced mixing of the aged aerosol layer with a recent nucleation event (Figure 10b). By the end of the leg, the Aitken contribution completely disappears and the particles become too small to serve as CCN at 0.2% S_c. Table 6 gives the average concentration of CN and CCN for each of these periods.

[28] CCN spectra are calculated for limiting cases of chemical composition using the average aerosol size distributions during the three selected time periods (Figures 10 a–10c) for various contributions of $(NH_4)_2SO_4$ in internal and external mixtures. Comparing size distributions to measured CCN concentrations (see section 3) provides insight on the chemistry of these aerosols. It is clear from these figures that aerosol size distributions have a first-order effect on the CCN spectra as expected from a sensitivity study by *Roberts et al.* [2002]. Figures 10b and 10c show the fraction of CCN-active aerosol decreased in the presence of a large ultrafine component. A comparison of the measured CCN concentrations in the aged aerosol layer to the limiting cases of CCN spectra (i.e., ammonium sulfate and insoluble, inactive particles) suggest an aerosol with <10% soluble mass content. These ratios are similar to chemical measurements of aged dust or biomass burning aerosol [*Gao et al.*, 1997; *Reid et al.*, 1998; *Zhang et al.*, 2003]. However, since the back trajectories indicate a source from northern China, the aged layer is probably associated to dust. In spite of the low-soluble content, this aged aerosol effectively behaves as CCN owing to its large size, yet vertical mixing is required to incorporate this aged,

Table 6. N_{CN}, N_{CCN}, $f_{CCN/CN}$ Corresponding to Different Types of Aerosols During the Horizontal Leg of Flight 15

	Aged Aerosol	Ultra Fine With Accumulation Mode	Ultra Fine
Time period	0 to 430 s	865 to1815 s	1990 to 2420 s
N_{CN}, cm^{-3}	523 ± 118	1292 ± 300	2300 ± 179
$N_{CCN,0.2}$ (CFS-CCN), cm^{-3}	294 ± 102	27 ± 13	1.8 ± 1.4
$f_{CCN/CN}$	0.54	0.026	10^{-3}
$N_{CCN,0.2}$ (STG-CCN), cm^{-3}	288 ± 48	...	...
$N_{CCN,0.4}$ (STG-CCN), cm^{-3}	243 ± 58	54 ± 30	...
$N_{CCN,0.8}$ (STG-CCN), cm^{-3}	355 ± 47	50 ± 21	...

long-range transport aerosol into the marine boundary layer to serve as CCN.

6. Conclusions

[29] An airborne experiment over the eastern Pacific Ocean measured multiple aerosol layers of long-range transport and highlighted the influence of physicochemical aerosol properties on CCN concentrations. The continuous flow streamwise thermal gradient (CFS-CCN) and static diffusion thermal gradient (STG-CCN) chambers show consistent results; however, the CFS-CCN instrument captures the effects of rapidly changing aerosol size distributions, emphasizing the importance of fast measurements for aircraft studies. A chemical transport model and back trajectories show that dust and anthropogenic emissions stretch from the Asia across the Pacific Ocean during this period. Vertical profiles near the coast of northern California reveal multiple layers of newly formed and aged aerosol. Six major aerosol types were observed during the experiment based on aerosol size distributions and back trajectories. These types include clean marine boundary layer aerosols, cloud-processed aerosols, North American continental aerosols, and three classes of long-range transport of Asian anthropogenic emissions. Our measurements show that new particle formation, characterized by high concentrations of particles <20 nm diameter, frequently occurs in thin stratified layers between 1000 and 7000 m asl. However, owing to their small size, the ultra-fine aerosols neither effectively scatter light nor immediately serve as CCN. In contrast, aged, long-range transport aerosols effectively scatter light and serve as CCN ($f_{CCN/CN}$ = 0.54; 0.2% S_c).

[30] The overall ratio of measured to predicted CCN concentration is 0.56±0.41 with a power law relationship of $N_{CCN,measured} = N_{CCN,predicted}^{0.846\pm0.002}$ for 23 research flights and 1884 comparisons. Our observations suggest this overprediction is a result of less CCN-active aerosol and can be explained by different aerosol types.

[31] CCN concentrations of cloud-processed aerosol were well predicted using an ammonium sulfate approximation for 0.3% S_c. The minima in the aerosol size distributions between 60 and 80 nm diameter, suggests in-cloud supersaturations near 0.3% during the experiment. Other aerosol types, especially North American continental aerosol and aged long-range transport aerosol, are less CCN active. We introduce a CCN activation index (ratio of critical diameter of ammonium sulfate to measured critical diameter at a given supersaturation) to assess the chemical effects in the absence of explicit chemical information. While the activation index cannot be determined solely on the basis of aerosol size distributions, a reasonable approximation can be established when considering back trajectory information. Cloud-processed aerosols exhibit an activation index closest to unity, while aged, long-range transport had values less than one third. In spite of the small amount of soluble mass of the aged, long-range transport, these aerosols effectively serve as CCN owing to their large size. Unless these aged layers are mixed into the boundary layer, these results suggest that such aerosol layers contribute more to the direct effect than the indirect effect during long-range transport.

[32] **Acknowledgments.** We thank Eric Wilcox and Carl Schmitt for their assistance as flight scientists and the University of Wyoming King Air flight crew for their hard work and dedication to this study. We also thank the National Science Foundation Atmospheric Sciences Program (ATM0201946) and the National Oceanic and Atmospheric Administration (NA17RJ1231-VR03) for their support of this research.

References

Bigg, E. K. (1986), Discrepancy between observation and prediction of concentrations of cloud condensation nuclei, *Atmos. Res.*, *20*, 81–86.

Bilde, M., and B. Svenningsson (2004), CCN activation of slightly soluble organics: The importance of small amounts of inorganic salt and particle phase, *Tellus, Ser. B*, *56*(2), 128–134.

Cantrell, W., G. Shaw, C. Leck, L. Granat, and H. Cachier (2000), Relationships between cloud condensation nuclei spectra and aerosol particles on a south-north transect of the Indian Ocean, *J. Geophys. Res.*, *105*(D12), 15,313–15,320.

Chuang, P. Y., D. R. Collins, H. Pawlowska, J. R. Snider, H. H. Jonsson, J. L. Brenguier, R. C. Flagan, and J. H. Seinfeld (2000), CCN measurements during ACE-2 and their relationship to cloud microphysical properties, *Tellus, Ser. B*, *52*(2), 843–867.

Collins, D. R., R. C. Flagan, and J. H. Seinfeld (2002), Improved inversion of scanning DMA data, *Aerosol Sci. Technol.*, *36*, 1–9.

Covert, D. S., J. L. Gras, A. Wiedensohler, and F. Stratmann (1998), Comparison of directly measured CCN with CCN modeled from the number-size distribution in the marine boundary layer during ACE 1 at Cape Grim, Tasmania, *J. Geophys. Res.*, *103*(D13), 16,597–16,608.

Delene, D. J., T. Deshler, P. Wechsler, and G. A. Vali (1998), A balloon-borne cloud condensation nuclei counter, *J. Geophys. Res.*, *103*(D8), 8927–8934.

Draxler, R. R., and G. D. Hess (1997), Description of the HYSPLIT_4 modeling system, *Tech. Memo. ERL ARL-224*, 24 pp., NOAA, Silver Spring, Md.

Feingold, G., and A. J. Heymsfield (1992), Parameterizations of condensational growth of droplets for use in general-circulation models, *J. Atmos. Sci.*, *49*, 2325–2342.

Feingold, G., and S. M. Kreidenweis (2002), Cloud processing of aerosol as modeled by a large eddy simulation with coupled microphysics and aqueous chemistry, *J. Geophys. Res.*, *107*(D23), 4687, doi:10.1029/2002JD002054.

Foltescu, V. L., E. Selin, and M. Below (1995), Corrections for particle losses and sizing errors during aircraft aerosol sampling using a rosemount inlet and the PMS LAS-X, *Atmos. Environ.*, *29*, 449–453.

Gao, Y., R. Arimoto, R. A. Duce, X. Y. Zhang, G. Y. Zhang, Z. S. An, L. Q. Chen, M. Y. Zhou, and D. Y. Gu (1997), Temporal and spatial distributions of dust and its deposition to the China Sea, *Tellus, Ser. B*, *49*(2), 172–189.

Garrett, T. J., and P. V. Hobbs (1995), Long-range transport of continental aerosols over the Atlantic Ocean and their effects on cloud structures, *J. Atmos. Sci.*, *52*, 2977–2984.

Hegg, D. A., L. F. Radke, and P. V. Hobbs (1990), Particle production associated with marine clouds, *J. Geophys. Res.*, *95*(D9), 13,917–13,926.

Hegg, D. A., L. F. Radke, and P. V. Hobbs (1991), Measurements of Aitken nuclei and cloud condensation nuclei in the marine atmosphere and their relation to the DMS-cloud-climate hypothesis, *J. Geophys. Res.*, *96*(D10), 18,727–18,733.

Hoppel, W. A., G. M. Frick, and R. E. Larson (1986), Effect of nonprecipitating clouds on the aerosol size distribution in the marine boundary layer, *Geophys. Res. Lett.*, *13*(1), 125–128.

Hudson, J. G. (1991), Observations of anthropogenic cloud condensation nuclei, *Atmos. Environ.*, *25*, 2449–2455.

Hudson, J. G. (1993), Cloud condensation nuclei near marine cumulus, *J. Geophys. Res.*, *98*(D2), 2693–2702.

Jaenicke, R. (1992), Vertical distribution of atmospheric aerosols, in *Nucleation and Atmospheric Aerosols*, edited by N. Fukuta, and P. E. Wagner, pp. 417–425, A. Deepak, Hampton, Va.

Kerminen, V.-M., and A. S. Wexler (1995), Enhanced formation, and development of sulfate particles due to marine boundary layer circulation, *J. Geophys Res.*, *100*(D11), 22,051–22,768.

Kline, J., B. Huebert, S. Howell, B. Blomquist, J. Zhuang, T. Bertram, and J. Carrillo (2004), Aerosol composition and size versus altitude measured from the C-130 during ACE-Asia, *J. Geophys. Res.*, *109*, D19S08, doi:10.1029/2004JD004540.

Köhler, H. (1936), The nucleus in and the growth of hygroscopic droplets, *Trans. Faraday Soc.*, *32*, 1152–1161.

Lala, G. G., and J. E. Jiusto (1977), An automatic light scattering CCN counter, *J. Appl. Meteorol.*, *16*, 413–418.

Liu, P. S. K., W. R. Leaitch, C. M. Banic, and S.-M. Li (1996), Aerosol observations at Chebogue Point during the 1 993 North Atlantic Regional Experiment: Relationships among cloud condensation nuclei, size distribution, and chemistry, *J. Geophys. Res.*, *101*(D22), 28,971–28,990.

Liu, Y. G., and P. H. Daum (2000), The effect of refractive index on size distributions and light scattering coefficients derived from optical particle counters, *J. Aerosol Sci.*, *31*(8), 945–957.

McNaughton, C. S., et al. (2004), Spatial distribution and size evolution of particles in Asian outflow: Significance of primary and secondary aerosols during ACE-Asia and TRACE-P, *J. Geophys. Res.*, *109*, D19S06, doi:10.1029/2003JD003528.

Nenes, A., P. Chuang, R. Flagan, and J. Seinfeld (2001), A theoretical analysis of cloud condensation nucleus (CCN) instruments, *J. Geophys. Res.*, *106*(D4), 3449–3474.

Pruppacher, H. R., and J. D. Klett (1997), *Microphysics of Clouds and Precipitation*, Springer, New York.

Raes, F., R. Van Dingenen, E. Vignati, J. Wilson, J. P. Putaud, J. H. Seinfeld, and P. Adams (2000), Formation and cycling of aerosols in the global troposphere, *Atmos. Environ.*, *34*, 4215–4240.

Ramanathan, V., et al. (2001), Indian Ocean Experiment: An integrated analysis of the climate forcing and effects of the great Indo-Asian haze, *J. Geophys. Res.*, *106*(D22), 28,371–28,398.

Reid, J. S., P. V. Hobbs, R. J. Ferek, D. R. Blake, J. V. Martins, M. R. Dunlap, and C. Liousse (1998), Physical, chemical, and optical properties of regional hazes dominated by smoke in Brazil, *J. Geophys. Res.*, *103*(D24), 32,059–32,080.

Roberts, G. (2001), Cloud condensation nuclei in the Amazon Basin: Their role in a tropical rainforest, Ph.D. thesis, Calif. Inst. of Technol., Pasadena.

Roberts, G., and A. Nenes (2005), A continuous-flow streamwise thermal-gradient CCN chamber for airborne measurements, *Aerosol Sci. Technol.*, *39*, 206–221.

Roberts, G. C., P. Artaxo, J. C. Zhou, E. Swietlicki, and M. O. Andreae (2002), Sensitivity of CCN spectra on chemical and physical properties of aerosol: A case study from the Amazon Basin, *J. Geophys. Res.*, *107*(D20), 8070, doi:10.1029/2001JD000583.

Roberts, G., A. Nenes, J. Seinfeld, and M. Andreae (2003), Impact of biomass burning on cloud properties in the Amazon Basin, *J. Geophys. Res.*, *108*(D2), 4062, doi:10.1029/2001JD000985.

Sano, I., S. Mukai, Y. Okada, B. N. Holben, S. Ohta, and T. Takamura (2003), Optical properties of aerosols during APEX and ACE-Asia experiments, *J. Geophys. Res.*, *108*(D23), 8649, doi:10.1029/2002JD003263.

Seinfeld, J. H., and S. N. Pandis (1998), *Atmospheric Chemistry and Physics: From Air Pollution to Climate Change*, 1326 pp., John Wiley, Hoboken, N. J.

Seinfeld, J. H., et al. (2004), ACE-ASIA—Regional climatic and atmospheric chemical effects of Asian dust and pollution, *Bull. Am. Meteorol. Soc.*, *85*(3), 367–380.

Shaw, R., and D. Lamb (1999), Experimental determination of the thermal accommodation and condensation coefficients of water, *J. Chem. Phys.*, *111*, 10,659–10,663.

Sinnarwalla, A., and D. Alofs (1973), A cloud nucleus counter with long available growth time, *J. Appl. Meteorol.*, *12*, 831–835.

Snider, J., and J. Brenguier (2000), Cloud condensation nuclei and cloud droplet measurements during ACE-2, *Tellus, Ser. B*, *52*, 828–842.

Squires, P. (1952), The growth of cloud drops by condensation, *Aust. J. Sci. Res.*, *A5*, 59–86.

Twomey, S. (1963), Measurements of natural cloud nuclei, *J. Rech. Atmos.*, *1*, 101–105.

Twomey, S. (1977), The influence of pollution on the short-wave albedo of clouds, *J. Atmos. Sci.*, *34*, 1149–1152.

Twomey, S., and P. Squires (1959), The influence of cloud nucleus population on the microstructure and stability of convective clouds, *Tellus*, *11*, 408–411.

Twomey, S., and J. Warner (1967), Comparison of measurements of cloud droplets and cloud nuclei, *J. Atmos. Sci.*, *24*, 702–703.

Uno, I., et al. (2003), Regional chemical weather forecasting system CFORS: Model descriptions and analysis of surface observations at Japanese island stations during the ACE-Asia experiment, *J. Geophys. Res.*, *108*(D23), 8668, doi:10.1029/2002JD002845.

VanCuren, R. A., S. S. Cliff, K. D. Perry, and M. Jimenez-Cruz (2005), Asian continental aerosol persistence above the marine boundary layer over the eastern North Pacific: Continuous aerosol measurements from Intercontinental Transport and Chemical Transformation 2002 (ITCT 2K2), *J. Geophys. Res.*, *110*, D09S90, doi:10.1029/2004JD004973.

Van Dingenen, R., F. Raes, J. P. Putaud, A. Virkkula, and M. Mangoni (1999), Processes determining the relationship between aerosol number and non-sea-salt sulfate mass concentrations in the clean and perturbed marine boundary layer, *J. Geophys. Res.*, *104*(D7), 8027–8038.

VanReken, T. M., T. A. Rissman, G. C. Roberts, V. Varutbangkul, H. H. Jonsson, R. C. Flagan, and J. H. Seinfeld (2003), Toward aerosol/cloud condensation nuclei (CCN) closure during CRYSTAL-FACE, *J. Geophys. Res.*, *108*(D20), 4633, doi:10.1029/2003JD003582.

Wang, S. C., and R. C. Flagan (1990), Scanning Electrical Mobility Spectrometer, *Aerosol Sci. Technol.*, *13*, 230–240.

Weber, R. J., et al. (2003), New particle formation in anthropogenic plumes advecting from Asia observed during TRACE-P, *J. Geophys. Res.*, *108*(D21), 8814, doi:10.1029/2002JD003112.

Wood, R., et al. (2000), Boundary layer and aerosol evolution during the third Lagrangian experiment of ACE-2, *Tellus, Ser. B*, *52*, 401–422.

Zhang, S. H., and R. C. Flagan (1996), Resolution of the radial differential mobility analyzer for ultrafine particles, *J. Aerosol Sci.*, *27*(8), 1179–1200.

Zhang, X. Y., S. L. Gong, R. Arimoto, Z. X. Shen, F. M. Mei, D. Wang, and Y. Cheng (2003), Characterization and temporal variation of Asian dust aerosol from a site in the northern Chinese deserts, *J. Atmos. Chem.*, *44*(3), 241–257.

O. Hadley, G. Mauger, V. Ramanathan, and G. Roberts, Center for Atmospheric Sciences Scripps Institution of Oceanography, 9500 Gilman Drive, Room 0239, La Jolla, CA 92093, USA. (greg@fiji.ucsd.edu)